JGR Atmospheres

RESEARCH ARTICLE
10.1029/2024JD041052

Special Collection:
Emerging air pollution: emissions, chemistry, and health and climate effects

Improving HONO Simulations and Evaluating Its Impacts on Secondary Pollution in the Yangtze River Delta Region, China

Haoran Zhang[1], Chuanhua Ren[1], Xueyu Zhou[1], Keqin Tang[2], Yuliang Liu[1], Tengyu Liu[1], Jiaping Wang[1], Xuguang Chi[1], Mengmeng Li[1], Nan Li[2], Xin Huang[1], and Aijun Ding[1]

[1]School of Atmospheric Sciences, Nanjing University, Nanjing, China, [2]Jiangsu Key Laboratory of Atmospheric Environment Monitoring and Pollution Control, Jiangsu Collaborative Innovation Center of Atmospheric Environment and Equipment Technology, School of Environmental Science and Engineering, Nanjing University of Information Science & Technology, Nanjing, China

Abstract Secondary air pollution, especially ozone (O_3) and secondary aerosols, are emerging air quality challenges confronting China. Nitrous acid (HONO), as the predominant source of hydroxyl radicals (OH), are acknowledged to be essential for secondary pollution. However, HONO concentrations are usually underestimated by current air quality models due to the inadequate representations of its sources. In the present study, we revised the Weather Research and Forecasting & Chemistry (WRF-Chem) model by incorporating additional HONO sources, including primary emissions, photo-/dark oxidation of NO_x, heterogeneous uptake of NO_2 on surfaces, and nitrate photolysis. By combining in-situ measurements in the Yangtze River Delta (YRD) region, we found the improved model show much better performance on HONO simulation and is capable of reproducing observed high concentrations. The source-oriented method is employed to quantitatively understand the relative importance of various processes, which showed that heterogeneous NO_2 uptake on the ground surface was the major contributor to HONO formation in urban areas. Comparatively, photo-oxidation of NO_x is a main contributor in rural areas. The introduction of multiple sources of HONO led to an apparent increase in OH and hydroperoxyl (HO_2) radicals. The promoted HO_2 levels further increased diurnal O_3 concentration by 4.5–12.9 ppb, while secondary inorganic and organic concentrations were also increased by 14%–32% during a typical secondary pollution event. The improved description of HONO emission and formation in the model substantially narrowed the gaps between simulations and observations, highlighting the great importance in understanding and numerical representations of HONO in secondary pollution study.

Plain Language Summary Nitrous acid (HONO) has a vigorous potential to produce hydroxyl radicals, contributing to tropospheric oxidation reactions. However, current air quality models lack detailed representation of HONO-related processes. We revised a widely-used air quality model based on recently reported mechanisms. The improved model can reasonably simulate actual HONO concentrations measured in the Yangtze River Delta region, one of the most urbanized city clusters in China. It is identified that the heterogeneous conversion of nitrogen dioxide on the ground surface and photo-oxidation of nitrogen oxide may play an important role in HONO formation. The modeling result is indicative of the pronounced enhancement of HONO on secondary air pollutants, including ozone and secondary aerosols. This study highlights the critical impact of HONO on deteriorating secondary air pollution in city clusters.

Key Points:

- Incorporating missing sources of HONO in the air quality model helps to better represent the observed magnitude and temporal variations of HONO
- Heterogeneous uptake of NO_2 on the ground surface and photo-oxidation of NO_x are major contributors to HONO formation
- HONO can significantly deteriorate ozone and secondary aerosol pollution by enhancing atmospheric oxidizing capacity

Supporting Information:

Supporting Information may be found in the online version of this article.

Correspondence to:

X. Huang,
xinhuang@nju.edu.cn

Citation:

Zhang, H., Ren, C., Zhou, X., Tang, K., Liu, Y., Liu, T., et al. (2024). Improving HONO simulations and evaluating its impacts on secondary pollution in the Yangtze River Delta region, China. *Journal of Geophysical Research: Atmospheres*, *129*, e2024JD041052. https://doi.org/10.1029/2024JD041052

Received 27 FEB 2024
Accepted 22 JUL 2024

Author Contributions:

Conceptualization: Xin Huang
Data curation: Haoran Zhang
Formal analysis: Haoran Zhang, Keqin Tang
Funding acquisition: Xin Huang, Aijun Ding
Investigation: Haoran Zhang, Chuanhua Ren, Xueyu Zhou, Yuliang Liu, Jiaping Wang, Xuguang Chi, Mengmeng Li, Nan Li
Methodology: Haoran Zhang
Project administration: Aijun Ding
Resources: Chuanhua Ren, Nan Li, Aijun Ding

1. Introduction

With the tremendous reduction in primary emissions over the past decade, secondary pollution from ozone (O_3) and secondary $PM_{2.5}$ has become an emerging threat to air quality in China (Fu et al., 2020; Huang et al., 2020; Lu et al., 2020; Wang, Wang, et al., 2023). Atmospheric oxidizing capacity (AOC) is dominant in modulating secondary pollution. It largely depends on the abundance of hydroxyl (OH) radicals (Wang, Li, et al., 2023). Nitrous acid (HONO) is one of the major precursors of tropospheric OH radicals. It is estimated that HONO accounts for approximately 20%–80% of OH production by self-photolysis, showing a vigorous potential in initiating atmospheric oxidation and the subsequent secondary pollution (Gu et al., 2022; Kim et al., 2014; Kleffmann et al., 2005; Slater et al., 2020; Su et al., 2008).

Software: Keqin Tang
Supervision: Xin Huang
Validation: Chuanhua Ren, Tengyu Liu
Visualization: Haoran Zhang
Writing – original draft: Haoran Zhang
Writing – review & editing: Haoran Zhang, Xueyu Zhou, Tengyu Liu, Mengmeng Li, Nan Li, Xin Huang

HONO can be directly emitted into the atmosphere from primary sources, including vehicle exhausts (Kurtenbach et al., 2001; Liao et al., 2021), agricultural soils (Oswald et al., 2013; Su et al., 2011; Xue et al., 2021; Zhang et al., 2023a), and wildfire plumes (Fredrickson et al., 2023; Nie et al., 2015; Theys et al., 2020). In addition, a most recent field study identified that livestock farming is an important but previously overlooked direct source of HONO in rural regions (Zhang et al., 2023a). Multiphase chemical reactions also significantly contribute to HONO formation. The most widely recognized pathway is the gas-phase reaction between NO and OH. Secondly, the illumination-enhanced heterogeneous uptake of NO_2 on solid surfaces serves as an important source as well (Chen et al., 2023; Finlayson-Pitts et al., 2003; Monge et al., 2010; Yu et al., 2022). Previous field measurements have reported that the heterogeneous uptake of NO_2 approximately accounts for 50% or more of HONO concentrations in China (Song et al., 2022; Ye et al., 2023; Zhang et al., 2022c, 2023b). Additionally, laboratory experiments suggest that particulate nitrate photolysis can produce HONO (Andersen et al., 2023; Ye et al., 2016, 2017). Apart from these formation pathways, a recent study proposed a novel mechanism unveiling HONO formation due to the photo-/dark-oxidation of nitrogen oxides ($NO_x = NO + NO_2$) (Song et al., 2023).

The representations of HONO sources in three-dimensional (3-D) chemical transport models (CTMs) are generally outdated. Most models only consider the homogeneous reaction pathway (NO + OH) to characterize HONO's formation, which fails to explain the high observed concentrations in the atmosphere (Sarwar et al., 2008). In order to bridge the gap between simulations and measurements, previous studies have attempted to incorporate additional HONO sources into CTMs. For instance, Li et al. (2010) implemented heterogeneous uptake of NO_2 on different surfaces in the Weather Research and Forecasting coupled with Chemistry (WRF-Chem) model. The revised model successfully reproduced the hourly variations of HONO and the relevant species O_3, OH, and hydroperoxyl (HO_2) radicals during the MCMA-2006/MILAGO observation campaign in Mexico City. Subsequently, this model was used to assess the impact of HONO on wintertime particulate pollution in the Beijing-Tianjin-Hebei (BTH) region and Guanzhong Plain of China (Li et al., 2022; Xing et al., 2019). Similar modeling studies were intensively conducted to improve HONO prediction and to quantify the associated environmental impacts on deteriorating O_3 and secondary aerosols in other Chinese regions, such as the North China Plain and Pearl River Delta (PRD) region (Fu et al., 2019; Tan et al., 2023; Zhang et al., 2016, 2019b, 2021, 2022a).

The Yangtze River Delta region (YRD) is one of the most highly urbanized and developed agglomerations in China, frequently suffering from secondary pollution (Li et al., 2023; Tang et al., 2022; Zhou et al., 2023). Previous studies on HONO sources in the YRD region are generally based on field measurements as well as laboratory experiments (Feng et al., 2023; Liu, Nie, et al., 2019; Ma et al., 2022; Zheng et al., 2020), while there is inadequate understanding in characterizing sources and sinks of HONO with 3-D CTMs. In this study, we incorporated primary emissions of HONO, heterogeneous uptake of NO_2 on solid surfaces, nitrate photolysis, and the newly presented photo-/dark-oxidation of NO_x into the WRF-Chem model. By integrating in-situ measurements in March 2019 with the revised numerical simulations, we quantified the improvement in model performance and analyzed the chemical budget of HONO. The improved model was further used to shed light on HONO's impacts on enhancing the formation of O_3 and secondary aerosols during a typical secondary pollution episode in the YRD region.

2. Data and Methods

2.1. Observational Site and Instrumentation

Continuous measurements were conducted from 20 to 29 March 2019 at the Station for Observing Regional Processes of the Earth System (SORPES, 32°07′ N, 118°57′ E; 62 m a.s.l.) located at the Xianlin Campus of Nanjing University in Nanjing, Jiangsu Province (Figure 1). SORPES station is situated in the central area of the YRD region and serves as a regional background station (Ding et al., 2016, 2019). Our study obtained hourly observations of gases (HONO, NO_x, O_3, carbon monoxide (CO)), aerosols ($PM_{2.5}$, SO_4^{2-}, NO_3^-, NH_4^+), and meteorological parameters during the study period. HONO concentrations were measured using a commercial long-path absorption photometer instrument (LOPAP) (Liu, Nie, et al., 2019). Trace gases, including NO_x, O_3, and CO, were measured with a chemiluminescence instrument (Thermo Fisher Scientific TEI 42i, TEI 49i, and TEI 48i). The $PM_{2.5}$ concentration was detected using a combined technique of light scattering photometry and β radiation attenuation (Thermo Fisher Scientific, Model 5030 SHARP, USA). Water-soluble aerosol ions, including SO_4^{2-}, NO_3^-, and NH_4^+ (SNA), were measured using the Monitor for Aerosols and Gases in ambient

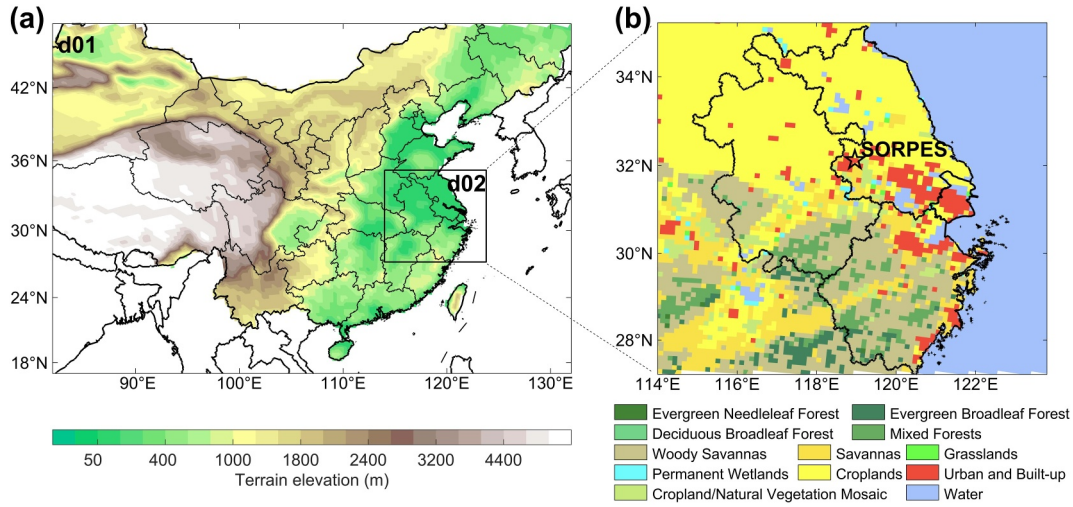

Figure 1. Illustration of the study regions in this study. Panel (a) shows the two modeling domains and the spatial distribution of terrain elevation. Panel (b) indicates the land use information over the nested domain 02 (d02), which covers the Yangtze River Delta region (black boundary). The pentagram in panel (b) stands for the SORPES station.

Air (MARGA; Metrohm, Switzerland) (Sun et al., 2018). Furthermore, an automatic weather station (CAMPEEL co., AG1000) simultaneously monitored meteorological parameters involving air temperature, relative humidity (RH), wind speed, and wind direction.

2.2. Chemical Transport Model

We utilized the WRF-Chem (v4.1.5) numerical modeling system to simulate the evolution of regional air pollution (Grell et al., 2005). The WRF-Chem model used the 1° × 1° FNL reanalysis data set (ds83.2) from the U. S. National Centers for Environmental Prediction (NCEP) as meteorological initial and boundary conditions. Additionally, four-dimensional data assimilation nudging technique was employed to improve meteorological simulation with upper and surface weather observations (ds351 and ds461). Various physical parameterizations were configured to model sub-grid processes, such as radiation transfer, boundary layer development, and microphysics (see Table S1 in Supporting Information S1). For chemistry, the Statewide Air Pollution Research Center (SAPRC99) mechanism (Carter, 2000) and the Model for Simulating Aerosol Interactions and Chemistry (MOSAIC) module (Zaveri et al., 2008) were applied to simulate trace gases and aerosols, respectively. Detailed information about the SAPRC99-MOSAIC mechanism in this study is provided in Text S1 in Supporting Information S1.

Our study configured two modeling domains. Figure 1 shows that the parent domain (d01) covers China with a horizontal resolution of 36 km × 36 km. The nested domain (d02) focuses on the YRD region with a grid spacing of 12 km. The vertical grids include 29 layers extending from the ground surface to the altitude of 50 hPa. To accurately capture diurnal variations in the atmospheric boundary layer, we designed 15 model layers below the altitude of 1 km. The anthropogenic emissions used in this study were obtained from the gridded Multi-resolution Emission Inventory for China (MEIC, v1.4) developed by Tsinghua University (Li et al., 2017). For d02, we merged the local emission inventory within the YRD region with a higher grid resolution of 4 km × 4 km (An et al., 2021). Biogenic emissions were calculated online using the Model of Emissions of Gases and Aerosols from Nature (MEGAN, v2.0.6) developed by Guenther et al. (2006).

2.3. Implementation of Multiple HONO Sources

2.3.1. Primary Emissions

The empirical ratio of HONO to NO_x (HONO/NO_x) is typically employed to estimate HONO emissions from combustion-related processes such as vehicular exhausts and industrial activities. The determination of HONO/NO_x relies on field measurements of freshly emitted plumes by applying the following criteria (Xu et al., 2015):

1. NO_x concentrations >40 ppb
2. $NO/NO_x > 0.85$ (ensuring predominant contribution from strong emissions)
3. A good correlation between HONO and NO_x with a correlation coefficient ($r > 0.9$)
4. Limited plume duration (<2 hr, minimizing aging effects on HONO)
5. UVB <0.01 Wm^{-2} (avoiding photochemistry reactions)
6. Lower wind speed and no precipitation (reducing meteorological influences)

Based on one-year continuous measurements at the SORPES station in Nanjing, Liu, Nie, et al. (2019) selected 55 freshly emitted plumes satisfying the criteria. The derived $HONO/NO_x$ ratios vary from 0.26% to 1.91%, with a mean value of 0.79% ± 0.36%. This ratio is generally consistent with previous results ranging from 0.78% to 0.85% (Kurtenbach et al., 2001; Liu et al., 2021; Xuan et al., 2023). Consequently, our model used an average ratio of 0.79% to approximate HONO primary emissions from combustion sources.

2.3.2. Heterogeneous Conversion of NO_2 on Surfaces

HONO produced via the heterogeneous reactive pathway includes the conversion on the ground surface (HET_LAND) and the aerosol surface (HET_AERO). As demonstrated in R1, the HONO yield was set to 0.5. The computation of the reactive kinetic rate for this heterogeneous reaction (k_{het}) can be simplified as a pseudo-first-order reaction. The calculation of k_{het_aero} and k_{het_land} follows Equations 1 and 2, respectively, where C_{NO2} represents the mean molecular velocity of NO_2 (m s^{-1}), further determined by Equation 3. R, T, and M_{NO2} in Equation 3 denote the ideal gas constant (8.314 J mol^{-1} K^{-1}), kelvin temperature (K), and the molar weight of NO_2 (46 g mol^{-1}). The parameter γ represents the dimensionless heterogeneous uptake coefficient. At night, γ for aerosol and ground surfaces are 8×10^{-6} and 4×10^{-6} (Zhang et al., 2021). Considering that illumination can efficiently promote the heterogeneous uptake of NO_2, the diurnal maxima of γ are expected to be 1×10^{-3} (γ_a) and 6×10^{-5} (γ_g) at noon (Liu, Lu, et al., 2019). The value γ_a is an upper limit compared to other similar studies (Fu et al., 2019; Li et al., 2010; Zhang et al., 2022a). To quantify the impact of this high uptake coefficient, we also conducted two additional sensitivity experiments using a γ_a of 1×10^{-4} and 1×10^{-5} (refer to Text S3 in Supporting Information S1). Results show that the uptake coefficient of 1×10^{-3} is acceptable. For other daytime hours, a dynamic linear scaling method presented by Song et al. (2023) was utilized in Equation 4 and Equation 5, where SR indicates solar radiation intensity (W m^{-2}).

S_a/V and S_g/V represent aerosol and ground surface area densities (m^2 m^{-3}). S_a/V was calculated using the MOSAIC aerosol model, which divided aerosols into four size bins ranging from 3.9 nm to 10 μm (Text S1 in Supporting Information S1). S_g/V was determined based on the underlying surface category. In regions with vegetation cover, S_g/V was estimated as the ratio of the double leaf area index (LAI, m^2 m^{-2}) to the height of the first layer in the WRF-Chem model (H, m). In our study, the first layer height was 41 m, close to the value (~35 m) reported in previous CTM modeling studies (Xue, 2022; Zhang et al., 2016, 2022a). For urban regions, the S_g/V ratio is empirically assumed to vary from 0.1 to 0.3 (Zhang et al., 2016). We constrained this parameter dynamically using a linear formula (Equation 6) based on the fraction of urban area so that highly urbanized regions can have more reactive surfaces. The original land use information in the WRF-Chem model is outdated. It cannot reflect the decadal urbanization changes in China. In order to tackle this issue, our study updated the land use information up to the level of 2019 (refer to Figure S1 in Supporting Information S1). The results showed a significant increase of 33% and 104% in the urban fraction and S_g/V within the SORPES station grid. It is important to note that the WRF-Chem model only accounts for NO_2 heterogeneous uptake by the ground surface within the first layer, while that on the aerosol surface is considered in all model layers (Zhang et al., 2016).

$$NO_2 + H_2O \rightarrow 0.5\ HNO_3 + 0.5\ HONO \quad \text{(R1)}$$

$$k_{het\_aero} = 0.25 \times C_{NO2} \times \gamma_a \times \frac{S_a}{V} \quad (1)$$

$$k_{het\_land} = 0.125 \times C_{NO2} \times \gamma_g \times \frac{S_g}{V} \quad (2)$$

$$C_{NO2} = \sqrt{\frac{8RT}{\pi M_{NO2}}} \quad (3)$$

$$\gamma_{a\_daytime} = 1 \times 10^{-3} \times \frac{SR}{1000} \quad (4)$$

$$\gamma_{g\_daytime} = 6 \times 10^{-5} \times \frac{SR}{1000} \quad (5)$$

$$\frac{S_g}{V} = \begin{cases} \frac{2LAI}{H} \ (vegetation) \\ 0.1 + 0.2 \times frac_{urban} \ (urban) \end{cases} \quad (6)$$

2.3.3. Particulate Nitrate Photolysis

During the daytime, particulate nitrate undergoes photolysis to produce HONO and NO_2. The molecular yields of these two products are 0.67 and 0.33 (R2), respectively. It was experimentally determined that the photolysis frequency of NO_3^- (J_{NO3-}) was 120 times higher than that of HNO_3 (J_{HNO3}) (Ye et al., 2017). However, it was argued that this rate had a high level of uncertainty and may lead to an overestimation in HONO concentrations. In this study, we adopted a moderate rate of J_{NO3-} (Equation 7) recommended by Zhang et al. (2022a).

$$NO_3^- + h\nu \rightarrow 0.67\ HONO + 0.33\ NO_2 \quad (R2)$$

$$J_{NO_3^-} = 30 \times J_{HNO3} \quad (7)$$

2.3.4. Photo-/Dark- Oxidation of NO_x

Recent smog chamber experiments have shown that NO_x oxidation may be a significant source of HONO formation (Song et al., 2023). After implementing this pathway into the CTM model, it was concluded that NO_x oxidation contributed to approximately over 40% of HONO production in Beijing, China. This formation pathway involves two reactions. During the daytime, HONO is generated due to the reaction between HNO_3 and NO (R3). Owing to the lack of the reaction order and rate constant, Song et al. (2023) represented the formation rate of R3 by multiplying the HNO_3 formation rate by 0.53 based on experimental data fitting (Equation 8). At night, HONO is produced by the dark-oxidation of NO_x, which involves the reaction between NO_3 radicals and NO. The dark-oxidation reaction is expressed through R4 with a 0.02 molecular yield of HONO.

$$HNO_3 + NO \rightarrow NO_2 + HONO \quad (R3)$$

$$\frac{d[HONO]}{dt} = 0.53 \times \frac{d[HNO_3]}{dt} + 0.00012\ \left(ppb\ s^{-1}\right) \quad (8)$$

$$NO_3 + NO \rightarrow 1.98\ NO_2 + 0.02\ HONO \quad (R4)$$

2.4. Source-Oriented Method

We used a source-oriented method (SOM) to reveal the contribution of each source and sink pathway to HONO concentrations. The SOM analysis in the WRF-Chem model is realized by configuring diagnostic variables to represent the contributions of different physical or chemical processes to species concentrations (Chen et al., 2019; Gao et al., 2020; Zhao et al., 2023). In our study, we defined seven source-tracking variables to track chemical sources from primary emissions (HONO_EMISS), homogeneous reaction between NO and OH (HONO_HOMO), photo-/dark-oxidation of NO_2 (HONO_PHOTO and HONO_DARK), heterogeneous uptake on the ground and aerosol surfaces (HONO_HETE_LAND and HONO_HETE_AERO), and photolysis of nitrate (HONO_PNO3_HV). Simultaneously, two sink-tracking variables were applied to reveal the removal intensity of HONO photodissociation (HONO_HV) and OH oxidation (HONO_OH). Specifically, the contribution of one HONO source or sink can be calculated by the difference between the concentration after the process calculation (C_{new}) and the concentration before the process calculation (C_{old}). Previous modeling studies often used brute-force methods (BFM) to identify source contributions (Song et al., 2023; Zhang et al., 2016, 2019a). However, BFM requires several sensitivity experiments, which can lead to extra computational burdens and potential biases (Liu et al., 2020). The SOM used in our study can track the individual contribution of each source to HONO formation within the same simulation.

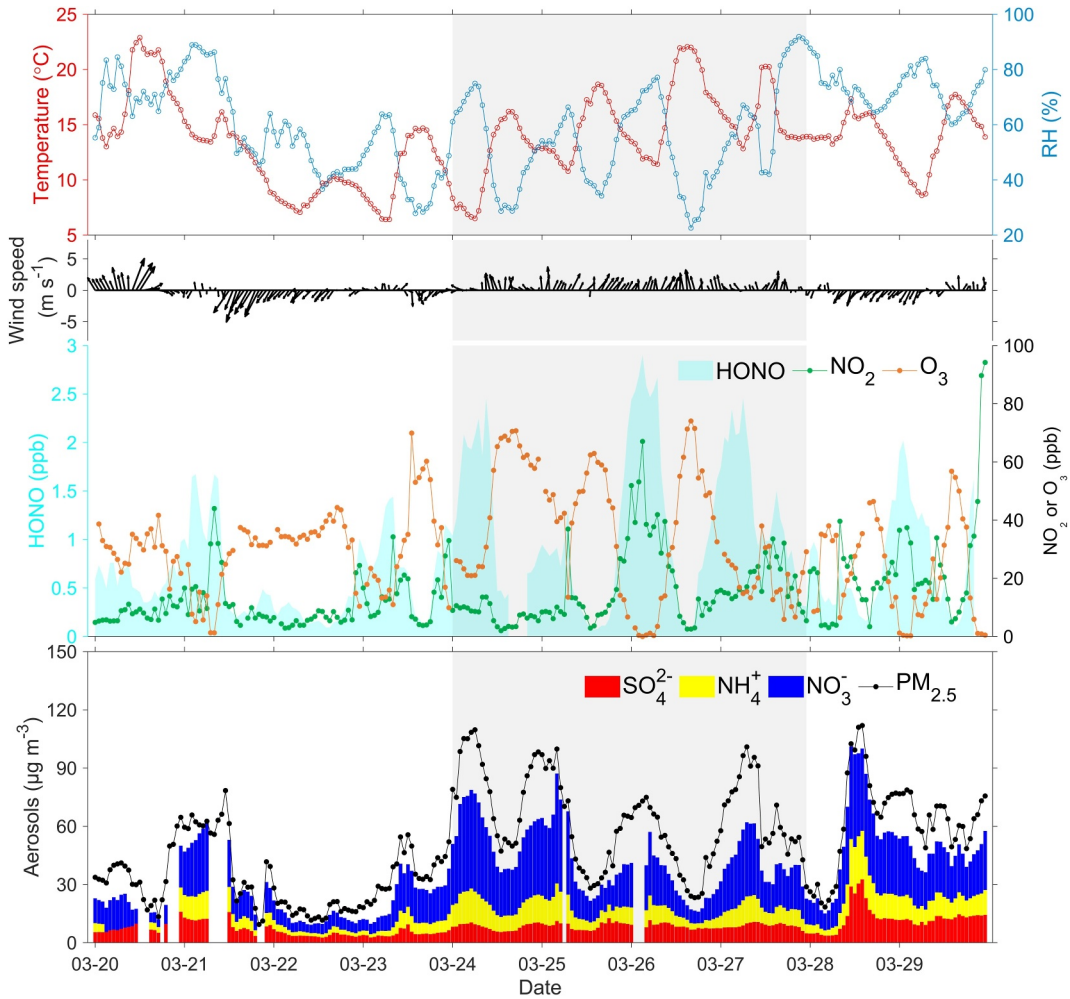

Figure 2. Time series of measurements of meteorological parameters (air temperature, relative humidity, wind speed, wind direction), trace gases (HONO, NO_2, O_3), and aerosols (SO_4^{2-}, NH_4^+, NO_3^-, total $PM_{2.5}$) at the SORPES station from 20 to 29 March 2019. The period showing the enhanced secondary pollution (24–27 March) is colored with gray shadows.

3. Results and Discussions

3.1. Observation on Elevated HONO and Secondary Pollution

Figure 2 shows the hourly variations of air pollutants and meteorological parameters measured at the SOPRES station during the study period. In general, an apparent increase in the concentrations of particulate aerosols (SO_4^{2-}, NH_4^+, NO_3^-, $PM_{2.5}$) and gaseous air pollutants (HONO and O_3) was observed from 24 to 27 March 2019. Among these species, $PM_{2.5}$ and HONO exhibited the most significant increase. According to the statistics in Table S2 in Supporting Information S1, the mean concentrations of $PM_{2.5}$ and HONO were 63.3 μg m^{-3} and 1.18 ppb, respectively, from 24 to 27 March. Compared with the previous period from 20 to 23 March, their relative elevation reached 89% and 100%, respectively.

By analyzing the synoptic weather, we found that the higher concentrations of air pollutants during March 24–27 can be attributed to unfavorable meteorological conditions. Figure 3a illustrates that the YRD region was under the control of the anticyclone system at 00:00 on 24 March. The high-pressure system near the ground surface led to stagnant atmospheric conditions that inhibited the diffusion of air pollutants (Cai et al., 2024; Zhou et al., 2023). At the same time, the weakened diffusion was also confirmed by the low wind speed at the SORPES station (Figure 2). Such a stable high-pressure pattern contributed to the dramatic increase in $PM_{2.5}$ concentration from 52.0 μg m^{-3} to 119.7 μg m^{-3} within the first 7 hr of 24 March. Daily $PM_{2.5}$ measurements from the national network showed severe haze pollution in the YRD region. Spatially, the high $PM_{2.5}$ levels were concentrated in

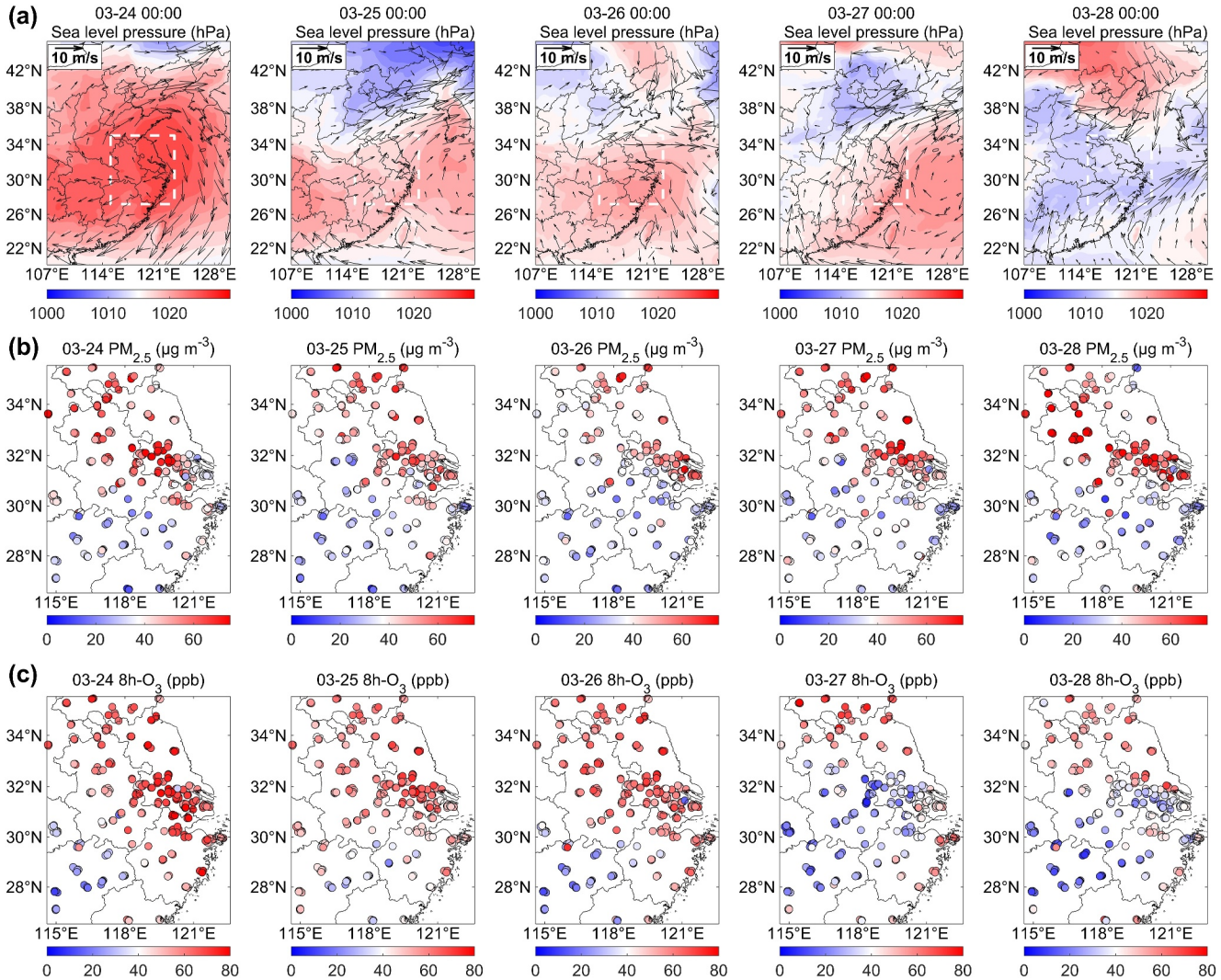

Figure 3. Spatial distributions of the background atmospheric circulation and air pollution from 24 to 28 March 2019. Panel (a) shows the surface sea level pressure (hPa) and 925 hPa wind field at 00:00 daily. The meteorological variables were obtained from ERA5 reanalysis data from the European Center for Medium-Range Weather Forecasts (ECMWF). The white dash rectangles stand for the Yangtze River Delta region. Panels (b, c) show the simultaneous spatial patterns of daily $PM_{2.5}$ (μg m^{-3}) and 8h-O_3 (ppb) concentrations from the Chinese National Environmental Monitoring Center (CNEMC).

the central and northern YRD region (Figure 3b). Subsequently, the anticyclone system gradually weakened and moved to the eastern oceanic areas of the YRD region. For the next 3 days (25–27 March), the YRD region was still influenced by the outer areas of this anticyclone system. $PM_{2.5}$ concentrations decreased slightly but remained at high levels. As a consequence of the effect of the anticyclone system, the average wind speed at the SORPES station from 24 to 27 March was 15% lower than that from 20 to 23 March, indicating reduced horizontal advection. In addition, the southerly wind persisted because the SOPRES station and the surrounding YRD region were west of the anticyclone system (Figures 2 and 3a). Previous studies often attributed the abrupt increase in $PM_{2.5}$ concentrations in the YRD region to the transport of pollutants from the upstream regions under the influence of a synoptic system such as a cold front (Kang et al., 2021; Liu et al., 2022). However, the $PM_{2.5}$ concentrations over the upstream regions were significantly lower than those in the YRD region (Figure 3b). Therefore, the inflow of cleaner air masses did not increase $PM_{2.5}$ concentrations and may help to dilute local pollution. The surface anticyclone system around the YRD region gradually dissipated after 27 March, changing the atmospheric circulation and the subsequent meteorological conditions (Figures 2 and 3a). On 28 March, northeasterly winds were observed at the SORPES station, demonstrating the return of airflows to local regions. Therefore, the observed $PM_{2.5}$ concentration at the SORPES station significantly increased.

Overall, the background atmospheric circulation demonstrated the weak contribution of transport from the upstream regions during March 24–27. In contrast, the observational evidence revealed a remarkable secondary production of $PM_{2.5}$ in the YRD region. Table S2 in Supporting Information S1 suggests that 56% of the concurrent increase in $PM_{2.5}$ can be attributed to the increase in SNA concentrations compared to 20–23 March. Figure S2 in Supporting Information S1 shows that water-soluble SNA ions accounted for 68% of the total $PM_{2.5}$ mass concentration during March 24–27. Among the inorganic ions, the concentration of NO_3^- was higher than the sum of SO_4^{2-} and NH_4^+, and its average increased from 13.6 μg m^{-3} to 24.8 μg m^{-3}. The rapid increase in NO_3^- concentration was partly due to the associated increase in precursor (NO_x) concentration. However, high nitrate yields were still observed on March 24–25, even under the lower NO_x condition (Figure S3 in Supporting Information S1). The enhanced AOC was probably a driving factor. This assumption can be further elucidated by the increase of the observed indicator ($PM_{2.5}$/CO), which reflects the secondary conversion efficiency (Huang et al., 2021). As summarized in Table S2 of the Supporting Information S1, the average $PM_{2.5}$/CO ratio from 24 to 27 March increased by 26% compared to the previous period (20–23 March). Simultaneously, the increase in O_3 also indicated an elevation in ambient AOC. The average 8h-O_3 concentration at the SORPES station increased by 29%. These high O_3 concentrations were also observed at numerous national monitoring sites throughout the YRD region (Figure 3c).

The significant increase in HONO concentration may explain the elevation in AOC levels. Due to the stagnation of the anticyclone system, HONO can easily accumulate under the circumstances of the lower wind speed. Moreover, the higher air temperature from 24 to 27 March (Figure 2 and Table S2 in Supporting Information S1) implies abundant solar radiation. Thus, the illumination-dependent heterogeneous uptake pathway can greatly enhance the HONO formation. Once formed, HONO subsequently contributed to the massive production of OH radicals via self-photolysis. The elevated OH concentrations can directly speed up the formation of gaseous precursors of secondary aerosols, including H_2SO_4 and HNO_3. Thus, concentrations of SNA aerosols significantly increased (Zhang et al., 2021). Additionally, the enhanced HO_x chemical cycle can further facilitate the generation of O_3 (Li et al., 2010). Consequently, O_3 can promote the oxidation processes of directly emitted air pollutants, leading to a rapid growth in SNA concentrations. This synergistic enhancement in O_3 and SNA initiated by HONO was previously confirmed in the PRD region by Fu et al. (2019). Given the dominant role of OH in governing AOC, we would like to quantify further the chemical role of HONO in amplifying secondary pollution during the observed typical secondary pollution event in the YRD region.

3.2. HONO Simulation Improvements and Process Diagnosis

In order to quantitively assess the contribution of HONO to the worsening of secondary pollution, it is essential to reproduce reasonable HONO concentrations with models in advance. In this section, we used the revised WRF-Chem model with complete representations of multiple HONO sources to simulate the observed high HONO concentrations at the SORPES station during March 24–27. The BASE scenario was the numerical experiment considering only the homogeneous reaction between NO and OH for HONO production. The other experimental simulation with four additional HONO sources was named the REVISED scenario.

3.2.1. Improvement in Modeling HONO Concentrations

First, we validated the HONO simulation with the in-situ measurements from the SORPES station. The measured HONO concentrations ranged from 0.04 to 2.90 ppb from 24 to 27 March, with a mean of 1.17 ppb. Consistent with previous field measurements, the peak HONO concentrations typically occurred at night (Feng et al., 2023; Zheng et al., 2020). The daytime HONO concentrations were lower due to its active photodissociation, with a minimum of 0.5 ppb. Figure 4a shows that the BASE simulation did not capture the magnitude of the observed HONO concentrations, particularly for the high nighttime values. By incorporating four additional sources into the model, the REVISED simulation showed a notable increase in the magnitude of the HONO concentration that closely matched the measurements (Figure 4b). The average HONO simulation increased from 0.07 ppb (BASE) to 1.24 ppb (REVISED). Simultaneously, the updated model also successfully reproduced the nocturnal HONO peaks. To quantify this improvement, we utilized three statistical metrics (Text S2 in Supporting Information S1), including the index of agreement (IOA), the normalized mean bias (NMB), and the root-mean-square error (RMSE). As summarized in Table 1, the IOA increased from 0.55 in the BASE simulation to 0.74 in the REVISED simulation, showing a significant improvement in agreement between simulation and observation. The NMB index changed from an underestimation of 94% to a slight overestimation of +6%. The RMSE in the

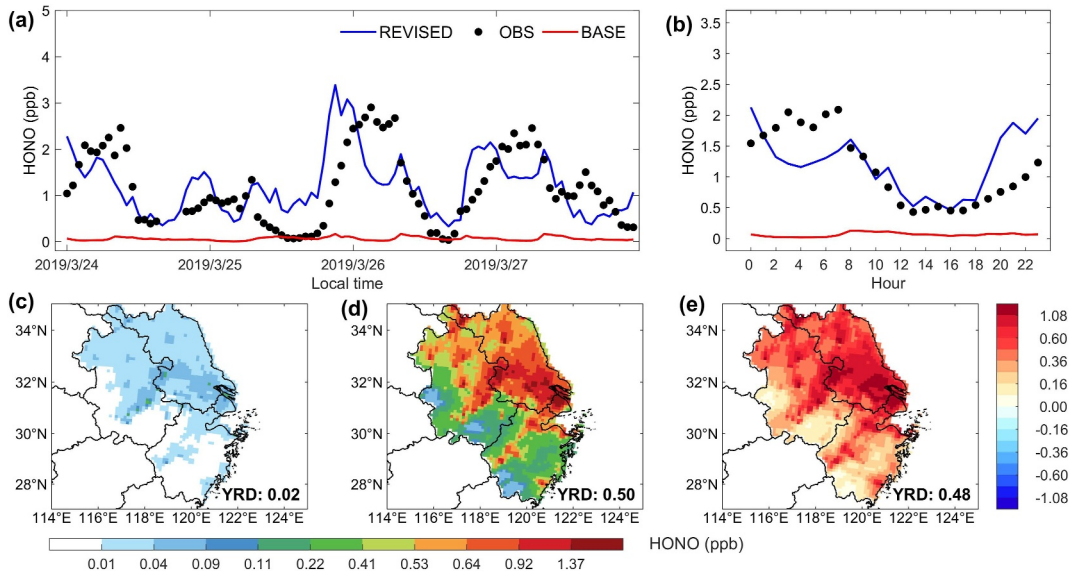

Figure 4. Model evaluation of HONO concentrations (ppb) in BASE scenario (NO + OH) and REVISED scenario (BASE plus four additional sources). Panels (a, b) show hourly and diurnal comparisons between model simulation and measurements. Panels (c–e) represent the spatial distribution of HONO concentrations in BASE, REVISED, and their differences (REVISED minus BASE). The regional mean value is marked in bold in each panel as well.

REVISED scenario was also reduced by 46% compared to the BASE scenario. These reductions in NMB and RMSE further confirm the improved biases in the HONO simulation. However, we still find a significant overestimation of 0.59 ∼ 1.03 ppb from 20:00 to 0:00. An underestimation of −0.84 ppb ∼ −0.47 ppb was also witnessed from 2:00 to 7:00. These biases may result from the parametrization uncertainties of HONO chemical sources working during the nighttime. Given that OH-consuming gaseous reactions and nitrate photolysis are inactive, the nighttime biases can be attributed to the uncertainties of the heterogeneous uptake on solid surfaces. The following section will give a detailed analysis of diurnal variations of the HONO chemical budget.

Furthermore, the HONO simulation also improved in the YRD region. As shown in Figure 4c, the average regional concentration of HONO in the BASE scenario was 0.02 ppb. Including complete representations of HONO sources led to an increase of 0.48 ppb (Figures 4d and 4e). Higher HONO concentrations were primarily found in the urban areas along the Yangtze River and Hangzhou Bay, where NO_x emissions are more prevalent due to the developed transportation (An et al., 2021). In contrast, the vegetation-covered southwest region of the YRD (as shown in Figure 1b) has significantly lower HONO concentrations due to its sparse NO_x emissions.

3.2.2. Analyses of HONO Chemical Budget

To better understand the formation process of HONO, we analyzed the contribution of each reactive pathway using SOM approach. Figure 5a illustrates that high HONO production rates occurred during the daytime, with a maximum of 12.7 ppb hr^{-1} at 11:00. This peak can be attributed to the substantial enhancement of light-related formation pathways, including the homogeneous reaction between NO and OH, photo-oxidation of NO_x, heterogeneous uptake of NO_2, and nitrate photolysis. The mean production rate during the daytime (from 7:00 to 18:00) was 7.70 ppb hr^{-1}. The dominant contributor to daytime HONO formation was the heterogeneous uptake of NO_2, which accounted for approximately 53% of the overall production rate. This finding is consistent with previous studies that have attributed heterogeneous NO_2 uptake to 43%–66% of daytime HONO production (Table S3 in Supporting Information S1). HETE_LAND was more significant, contributing 47% to the daytime production rate of HONO, while HETE_AERO only accounted for 6%. The discrepancy in two heterogeneous reactions results from the large difference in the surface area density. At the SORPES station, our simulation estimated the average density of aerosol surface area to be

Table 1
Metrics of Model Evaluation in Simulating HONO Concentrations

	BASE	REVISED
Observation (ppb)	1.17	1.17
Simulation (ppb)	0.07	1.24
IOA	0.55	0.74
NMB	−94%	6%
RMSE	1.36	0.74

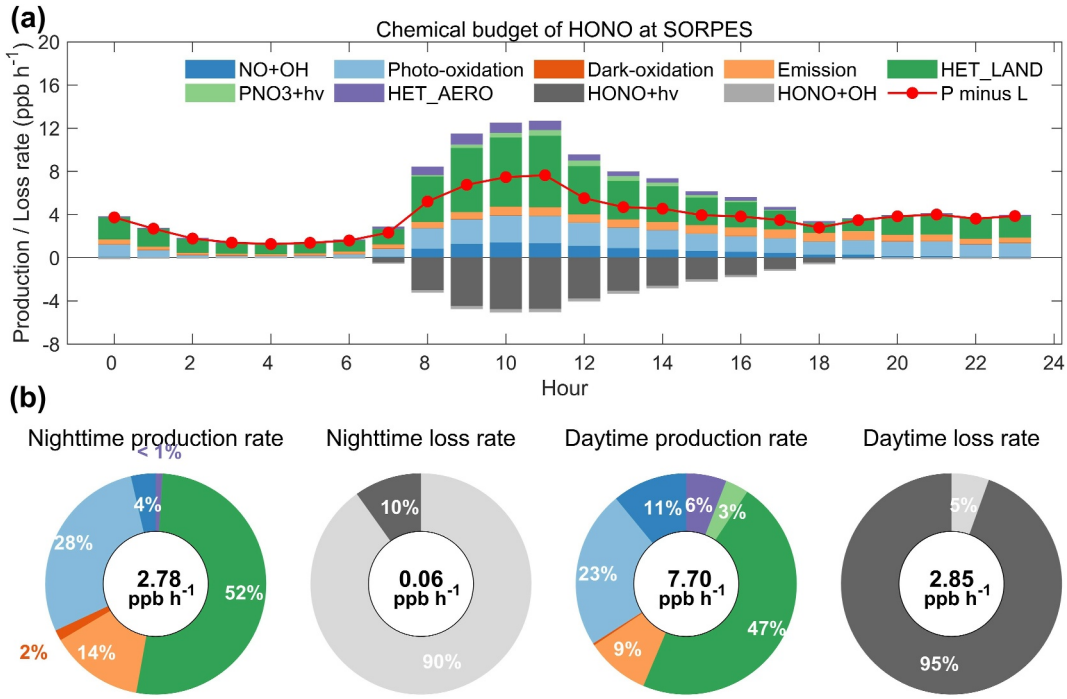

Figure 5. Chemical sources and sinks of HONO at the SORPES station (ppb h^{-1}). Panel (a) shows the diurnal variations of the production (P) and loss (L) rates of seven formation pathways (NO + OH, Photo-oxidation, Dark-oxidation, Emission, HET_LAND, PNO3 + hv, and HET_AERO) and two loss pathways (HONO + hv and HONO + OH). The net chemical formation rate is derived by deducting the loss rate from the formation rate (P–L). Panel (b) shows the relative contribution of each pathway during the daytime (7:00 to 18:00) and nighttime (19:00 to 6:00).

6.7×10^{-4} m^2 m^{-3}, which was notably lower (by 2–3 orders of magnitude) than the assumed area density on the ground surface (1.6×10^{-1} m^2 m^{-3}). In addition, we found that during the daytime, photo-oxidation of NO_x, the homogeneous reaction, primary emissions, and nitrate photolysis contributed 23%, 11%, 9%, and 3%, respectively, to the HONO formation. These results are comparable to previously reported ranges, as shown in Table S3 of Supporting Information S1. During the nighttime (19:00 to 6:00), the mean production rate of HONO was 2.78 ppb hr^{-1}, which is 64% lower than during the daytime. The dominant source in nocturnal HONO formation was HETE_LAND, which contributed 52%. HETE_AERO had a lower contribution (<1%) to HONO due to the decreased reactive uptake coefficient at night. The overall contribution of the two types of heterogeneous reactions remained nearly the same during both daytime and nighttime. Compared to the daytime, the contributions of photo-/dark-oxidation of NO_x and primary emissions to HONO formation present a significant increase at night, with their percentages being 30% and 14%, respectively. Meanwhile, the relative contributions of the homogeneous reaction and nitrate photolysis show a notable decrease due to the lower photochemical reactivity.

The considerable contribution of the heterogeneous uptake of NO_2 on the ground surface to HONO formation at the SORPES station resulted from the following three aspects. The first cause is the property of the urban underlying surface (Figure 1b), which provides a more available reaction area for the heterogeneous uptake. The other is the effect of the meteorological condition. As illustrated in Section 3.1, the temperature was higher during March 24–27 under the control of the ground high-pressure system. The solar radiation was abundant, with its maximum intensity up to 900 Wm^{-2} at 11:00 (see Figure S4 in Supporting Information S1). Therefore, the heterogeneous process was significantly enhanced by increasing the light-dependent uptake coefficient. Moreover, the southwesterly wind driven by the anticyclone system transported NO_x from the downtown area of Nanjing to the SORPES station, which supplied enough precursors for further conversion to HONO (Xia et al., 2020).

HONO can be lost through self-photolysis and OH-oxidation depletion. We show the diurnal variation of the associated chemical losses at the SORPES station in Figure 5. The two removal reactions were generally regulated by radiation intensity and only active during the daytime. These loss reactions were regulated by radiation

Table 2
HONO Production Rates (ppb h^{-1}) and Relative Contributions (%) of Different Pathways in Urban and Rural Areas of the YRD Region

	YRD region		Urban		Rural	
Total production rate	1.275		3.732		1.063	
NO + OH	0.137	(11%)	0.270	(7%)	0.128	(12%)
Photo-oxidation	0.358	(28%)	0.694	(19%)	0.331	(31%)
Dark-oxidation	0.012	(<1%)	0.022	(<1%)	0.012	(1%)
Emissions	0.092	(7%)	0.279	(7%)	0.076	(7%)
HET_LAND	0.431	(34%)	2.148	(58%)	0.277	(26%)
PNO3 + hv	0.124	(10%)	0.129	(3%)	0.122	(11%)
HET_AERO	0.121	(9%)	0.190	(5%)	0.117	(11%)

intensity and only active during the daytime (Figure 5). The average loss rate during the daytime was 2.85 ppb hr^{-1}, with 95% attributed to HONO photolysis. The net chemical formation rate peaked at 7.6 ppb hr^{-1} at 11:00. Then, production and loss rates decreased due to the weakened radiation intensity.

Figure S5 in Supporting Information S1 exhibits the HONO production rate of each source on a larger spatial scale. Except for nitrate photolysis, the spatial distribution pattern of production rates for all pathways is generally consistent with that of NO_x (Figure S6a in Supporting Information S1). The production rate resulting from nitrate photolysis follows the concentration levels of nitrate (Figure S6b in Supporting Information S1). Simultaneously, the chemical sources of HONO propose distinct composition characteristics between urban and rural areas in the YRD region. As listed in Table 2, the overall production rate of HONO formation was 3.732 ppb hr^{-1} in urban areas, which is three times higher than in rural areas. However, the lack of primary emissions from agricultural sectors such as soil and livestock may lead to underestimating the HONO formation rate in rural areas over the YRD region. Therefore, the difference between urban and rural could be smaller than expected. The higher formation potential of HONO in the urban areas highlights the more important enhancement in the subsequent secondary pollution compared to the rural areas. This difference in HONO formation rate between urban and rural areas is mainly due to NO_x abundance. Additionally, the higher density of ground surface area in urban areas facilitates the heterogeneous uptake of NO_2. The HET_LAND pathway was the dominant chemical source for urban HONO, contributing to 58% of the total production rate. However, this pathway's contribution was lower in rural regions (26%). On the contrary, the photo-oxidation of NO_x was the predominant source of rural HONO formation, with a relative contribution of 31%. Furthermore, in comparison to urban areas, the production rate of HONO was influenced more significantly by the homogeneous reaction between NO and OH, nitrate photolysis, and HETE_AERO. The overall average production rate in the YRD region was 1.275 ppb hr^{-1}. The contribution of each source, in descending order, is as follows: 34% for NO_2 heterogeneous uptake on the ground surface, 28% for photo-oxidation of NO_x, 11% for the homogeneous reaction, 10% for nitrate photolysis, 9% for NO_2 heterogeneous uptake on the aerosol surface, 7% for primary emissions.

3.3. Impacts of HONO on Secondary Pollution

As a consequence of the increase in HONO concentrations, the ambient AOC was also enhanced. Figure 6b shows that the average concentration of OH radical increased significantly from 1.4×10^6 molecule cm^{-3} in the BASE scenario to 2.8×10^6 molecule cm^{-3} in the REVISED scenario. This increase was particularly noticeable in the morning, with the maximum relative rise of 204% at 8:00. This phenomenon aligns with the modeling results previously presented by Fu et al. (2019). It is attributed to the dominant role of HONO in producing OH radicals in the early morning when O_3-related OH production has not yet efficiently worked. Due to the rapid interconversion of HO_x, concentrations of HO_2 radicals were also elevated, resulting in a 58% increase compared to the BASE scenario (Figure 6c). According to the O_3 photochemical regime, HO_2 can replace O_3 to react with NO (Li et al., 2019; Wang et al., 2017). Therefore, the substantial increase of HO_2 radicals further facilitated the accumulation of O_3. Figure 6a shows that the daily maxima of O_3 went through an evident increase. Excluding the simulated results on 27 March, when the model significantly overestimated, the average 8h-O_3 concentration on other days increased from 51.5 ppb (BASE) to 63.8 ppb (REVISED). The increased O_3 concentration was closer to the observation (62.0 ppb), further indicating an improvement in O_3 simulation. The diurnal increase in O_3 concentration caused by HONO varied from 4.5 ppb (7:00) to 12.9 ppb (12:00). As depicted in Figure S7 of the Supporting Information S1, this range is consistent with the findings of previous studies (3.8–14.8 ppb) (Zhang et al., 2022b). In conclusion, the increase of both O_3 and HO_x radicals exhibited a remarkable enhancement of the ambient AOC condition.

The enhanced AOC subsequently influenced the formation of secondary aerosols. We used the sulfur oxidation ratio (SOR) and nitrogen oxidation ratio (NOR) to reflect the enhancement of SO_4^{2-} and NO_3^-, respectively. These indicators have been widely used in previous studies (Chang et al., 2020; Ji et al., 2018) and were calculated using Equations 9 and 10, where *n* denotes the molar fraction. Figure S8 in Supporting Information S1 shows that both SOR and NOR exhibit higher varying ranges in the REVISED scenario compared to the BASE scenario.

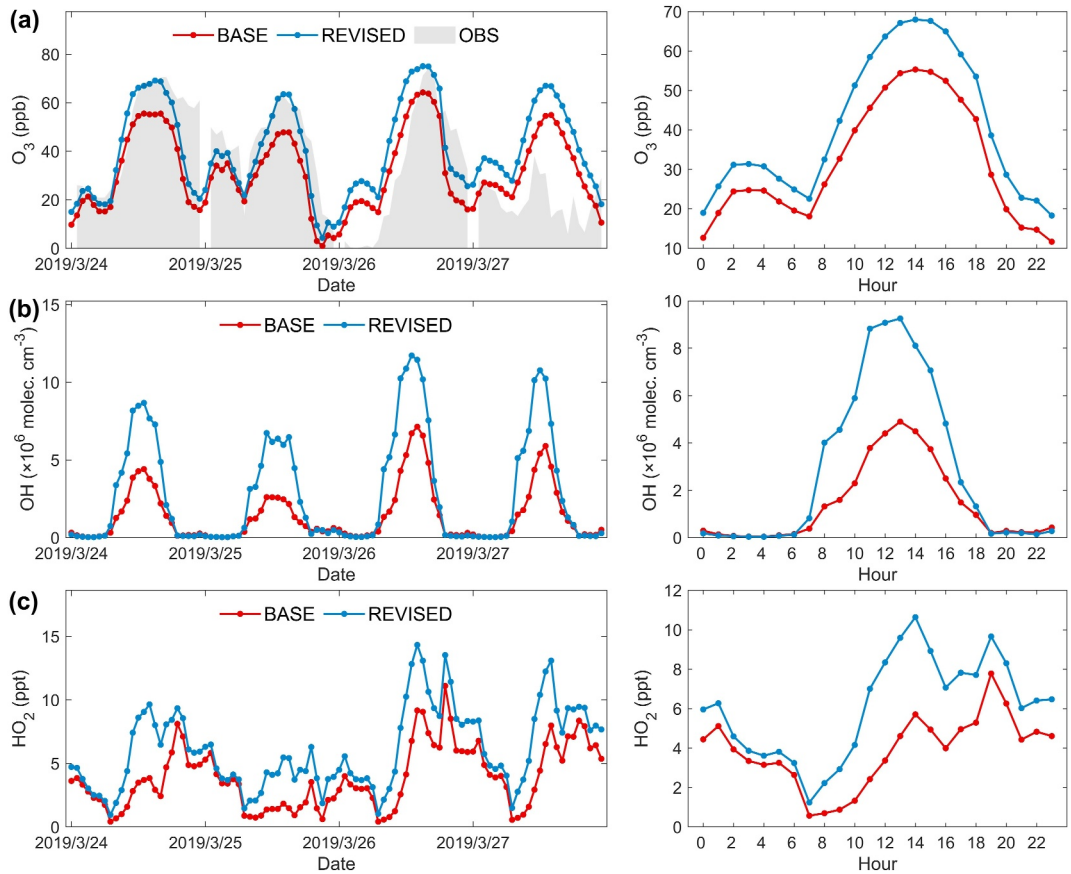

Figure 6. Comparisons between BASE and REVISED in simulating (a) O_3 (ppb), (b) OH radicals ($\times 10^6$ molecule cm^{-3}), and (c) HO_2 radicals (ppt) at the SORPES station. The left panels show the hourly variations, where O_3 measurements are exhibited with gray shadows. The right panels illustrate the diurnal variations.

Notably, there was a more significant relative increase in average NOR (34%), while SOR showed a rise of 19%. For NOR, apart from the enhanced secondary conversion, the depletion of NO_2 during HONO generation also led to the increase of NOR.

$$SOR = \frac{n[SO_4^{2-}]}{n[SO_4^{2-}] + n[SO_2]} \tag{9}$$

$$NOR = \frac{n[NO_3^-]}{n[NO_3^-] + n[NO_2]} \tag{10}$$

Simultaneously, SNA concentrations showed an associated enhancement. Figure 7a illustrates that in the REVISED scenario, the average concentrations of SO_4^{2-}, NO_3^-, and NH_4^+ increased by 24%, 32%, and 30%, respectively. In the BASE scenario, WRF-Chem simulations failed to capture the magnitude of SNA concentration accurately. Incorporating the enhanced secondary production contributed by HONO can reduce the underestimation of simulating SNA species. The improvement in model performance was particularly significant for NH_4NO_3, as its average concentration increased from 21.4 μg m^{-3} (BASE) to 28.0 μg m^{-3} (REVISED), presenting a reduced bias against the measurement (34.5 μg m^{-3}). The concentrations of secondary organic aerosols (SOA) also increased. Our model simulated the evolution of SOA from semi-/intermediate volatile organic compounds (SI-VOCs) and anthropogenic and biogenic VOCs (AB-VOCs), with their corresponding products named SI-SOA and AB-SOA, respectively. Consistent with previous findings (Feng et al., 2016; Miao et al., 2021), SI-SOA contributed more (~80%) to the total SOA concentration in both scenarios. Implementing multiple sources of HONO resulted in an average rise of 2.5 μg m^{-3} in total SOA concentration (Figure 7b).

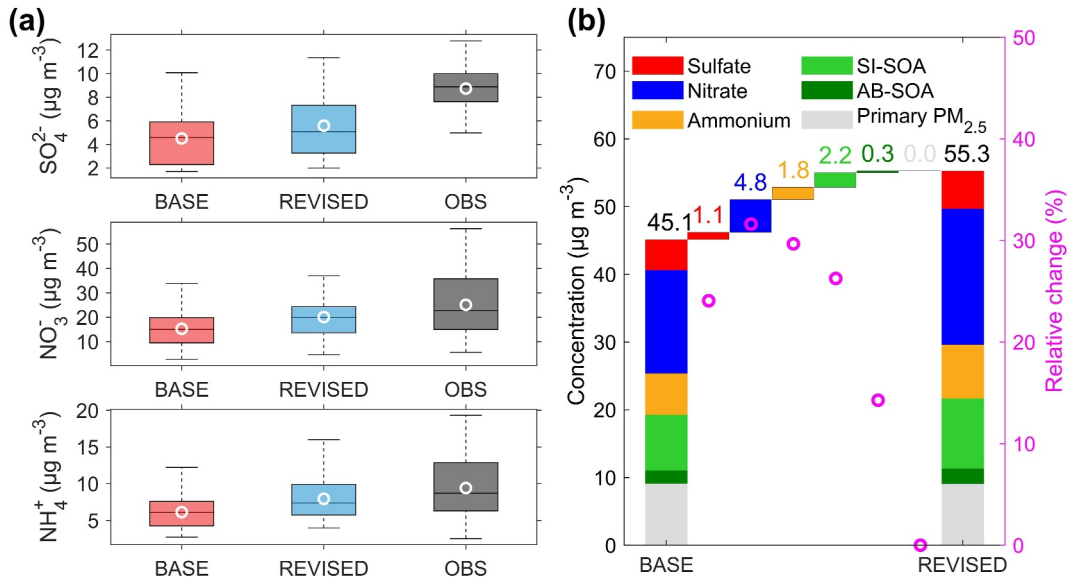

Figure 7. Enhancement of secondary aerosol concentrations in the BASE and REVISED scenarios. Panel (a) shows the box-whisker plots of SNA aerosol concentrations (μg m^{-3}). The white circles stand for the average concentration. Panel (b) exhibits the comparison between BASE versus REVISED in the $PM_{2.5}$ chemical composition. SI-SOA and AB-SOA denote SOA contributed by the oxidation of S/IVOCs and anthropogenic/biogenic VOC precursors, respectively. The pink circles represent relative aerosol concentration changes (%).

Approximately 88% of the SOA increase was attributed to the oxidation of semi-/intermediate VOCs. The relatively larger increase in SI-SOA (26%) compared to AB-SOA (14%) indicates a more positive response of SI-VOCs to AOC enhancement. On the other hand, primary $PM_{2.5}$ components (sum of elemental carbon, primary organic aerosols, and mineral dust) did not change. The shifts in secondary aerosols led to a net increase of 22% in $PM_{2.5}$ concentration. Overall, the proportion of secondary $PM_{2.5}$ increased from 80% to 84%, posing a further extent of secondary aerosol pollution.

4. Conclusions

To improve the severe underestimation of HONO in the standard WRF-Chem model, we incorporated four additional important sources, including observation-based primary emissions, newly presented photo-/dark-oxidation of NO_x, heterogeneous uptake of NO_2 on surfaces, and nitrate photolysis. The revised model successfully captured the magnitude and temporal variations of the observed HONO. Using the improved WRF-Chem model and comprehensive measurements at the SORPES station, our work investigated the HONO formation and its role in the deterioration of O_3 and secondary aerosols during a typical secondary pollution episode in the YRD region.

Observational evidence indicated that the stagnant meteorological conditions facilitated the accumulation of polluted air masses. HONO concentrations were notably elevated due to the lower wind speed. Moreover, the source analysis further revealed that the heterogeneous uptake of NO_2 on the ground surface (47%–52%) was the major contributor to HONO at the SORPES station due to the higher surface area density in the urban underlying surface. The adequate solar radiation and potential transport of NO_x from downtown Nanjing also contributed to the significant production of the heterogeneous reaction. By contrast, the contribution of photo-oxidation of NO_x was more significant to HONO in rural areas of the YRD region (31%). The three times higher HONO production rate in urban areas than in rural areas implies a higher potential for secondary pollution in densely populated regions.

The elevated HONO levels led to the rise of concentrations of OH and HO_2 radicals. As a result, the diurnal O_3 concentration significantly increased by 4.5–12.9 ppb. The HONO enhancement also increased secondary inorganic and organic aerosol concentrations by 14%–32%. In contrast, primary $PM_{2.5}$ concentrations did not change. The increase in secondary aerosols led to a net rise in total $PM_{2.5}$ by 22%. Simultaneously, the

improvement in the description of HONO sources also effectively reduced the model underestimation of secondary air pollutants, including O_3 and SNA. Overall, our work highlights the critical effect of HONO in driving regional secondary pollution. Further understanding of their parameterizations should be continuously developed and incorporated into the CTMs in the future.

Conflict of Interest

The authors declare no conflicts of interest relevant to this study.

Data Availability Statement

The WRF-Chem model is open-source air quality model from UCAR (https://www2.mmm.ucar.edu/wrf/users/). Meteorological input data for the WRF-Chem model were derived from NOAA public databases (https://rda.ucar.edu/datasets/). Anthropogenic emissions were obtained from public website of MEIC (http://meicmodel.org.cn/). YRD specific emissions were collected from An et al. (2021). The national air quality monitoring data are archived at a repository of Chinese National Environmental Monitoring Center (http://www.cnemc.cn/sssj/). The ERA5 reanalysis data were obtained from ECMWF (Hersbach et al., 2023). The HONO data is archived on the Figshare platform at (Zhang & Huang, 2024). Figures in this article are processed with MATLAB Release 2023b.

Acknowledgments
This work was supported by the National Natural Science Foundation of China (42293322), the National Key Research and Development Program of China (2022YFC3701105 and 2023YFC3709401) and the Comprehensive Observation and Research Project on Atmospheric Pollution in the Meizhou Bay Region.

References

An, J., Huang, Y., Huang, C., Wang, X., Yan, R., Wang, Q., et al. (2021). Emission inventory of air pollutants and chemical speciation for specific anthropogenic sources based on local measurements in the Yangtze River Delta region, China. *Atmospheric Chemistry and Physics*, *21*(3), 2003–2025. https://doi.org/10.5194/acp-21-2003-2021

Andersen, S. T., Carpenter, L. J., Reed, C., Lee, J. D., Chance, R., Sherwen, T., et al. (2023). Extensive field evidence for the release of HONO from the photolysis of nitrate aerosols. *Science Advances*, *9*(3), eadd6266. https://doi.org/10.1126/sciadv.add6266

Cai, S., Liu, T., Huang, X., Song, Y., Wang, T., Sun, Z., et al. (2024). Important role of low cloud and Fog in sulfate aerosol formation during winter haze over the North China plain. *Geophysical Research Letters*, *51*(3), e2023GL106597. https://doi.org/10.1029/2023GL106597

Carter, W. P. L. (2000). Documentation of the SAPRC-99 chemical mechanism for VOC reactivity assessment. Report to the California Air resources Board, Contracts 92-329 and 95-308.

Chang, Y., Huang, R., Ge, X., Huang, X., Hu, J., Duan, Y., et al. (2020). Puzzling haze events in China during the coronavirus (COVID-19) shutdown. *Geophysical Research Letters*, *47*(12). https://doi.org/10.1029/2020GL088533

Chen, J., Jiang, H., Chen, X., Wang, J., Huang, D., Lian, C., et al. (2023). A novel mechanism for NO2-to-HONO conversion on soot: Synergistic effect of elemental carbon and organic carbon. *Environmental Science and Technology Letters*, *10*, 878–884. https://doi.org/10.1021/acs.estlett.3c00624

Chen, L., Zhu, J., Liao, H., Gao, Y., Qiu, Y., Zhang, M., et al. (2019). Assessing the formation and evolution mechanisms of severe haze pollution in the Beijing–Tianjin–Hebei region using process analysis. *Atmospheric Chemistry and Physics*, *19*(16), 10845–10864. https://doi.org/10.5194/acp-19-10845-2019

Ding, A., Huang, X., Nie, W., Chi, X., Xu, Z., Zheng, L., et al. (2019). Significant reduction of PM2.5 in eastern China due to regional-scale emission control: Evidence from SORPES in 2011–2018. *Atmospheric Chemistry and Physics*, *19*(18), 11791–11801. https://doi.org/10.5194/acp-19-11791-2019

Ding, A., Nie, W., Huang, X., Chi, X., Sun, J., Kerminen, V.-M., et al. (2016). Long-term observation of air pollution-weather/climate interactions at the SORPES station: A review and outlook. *Frontiers of Environmental Science & Engineering*, *10*(5), 15. https://doi.org/10.1007/s11783-016-0877-3

Feng, J., Ren, E., Hu, M., Fu, Q., Duan, Y., Huang, C., et al. (2023). Budget of atmospheric nitrous acid (HONO) during the haze and clean periods in Shanghai: Importance of heterogeneous reactions. *Science of the Total Environment*, *900*, 165717. https://doi.org/10.1016/j.scitotenv.2023.165717

Feng, T., Li, G., Cao, J., Bei, N., Shen, Z., Zhou, W., et al. (2016). Simulations of organic aerosol concentrations during springtime in the Guanzhong Basin, China. *Atmospheric Chemistry and Physics*, *16*(15), 10045–10061. https://doi.org/10.5194/acp-16-10045-2016

Finlayson-Pitts, B. J., Wingen, L. M., Sumner, A. L., Syomin, D., & Ramazan, K. A. (2003). The heterogeneous hydrolysis of NO_2 in laboratory systems and in outdoor and indoor atmospheres: An integrated mechanism. *Physical Chemistry Chemical Physics*, *5*(2), 223–242. https://doi.org/10.1039/B208564J

Fredrickson, C. D., Theys, N., & Thornton, J. A. (2023). Satellite evidence of HONO/NO_2 increase with fire radiative power. *Geophysical Research Letters*, *50*(17), e2023GL103836. https://doi.org/10.1029/2023GL103836

Fu, X., Wang, T., Gao, J., Wang, P., Liu, Y., Wang, S., et al. (2020). Persistent heavy winter nitrate pollution driven by increased photochemical oxidants in northern China. *Environmental Science and Technology*, *54*(7), 3881–3889. https://doi.org/10.1021/acs.est.9b07248

Fu, X., Wang, T., Zhang, L., Li, Q., Wang, Z., Xia, M., et al. (2019). The significant contribution of HONO to secondary pollutants during a severe winter pollution event in southern China. *Atmospheric Chemistry and Physics*, *19*, 1–14. https://doi.org/10.5194/acp-19-1-2019

Gao, J., Li, Y., Zhu, B., Hu, B., Wang, L., & Bao, F. (2020). What have we missed when studying the impact of aerosols on surface ozone via changing photolysis rates? *Atmospheric Chemistry and Physics*, *20*(18), 10831–10844. https://doi.org/10.5194/acp-20-10831-2020

Grell, G. A., Peckham, S. E., Schmitz, R., McKeen, S. A., Frost, G., Skamarock, W. C., & Eder, B. (2005). Fully coupled "online" chemistry within the WRF model. *Atmospheric Environment*, *39*(37), 6957–6975. https://doi.org/10.1016/j.atmosenv.2005.04.027

Gu, R., Shen, H., Xue, L., Wang, T., Gao, J., Li, H., et al. (2022). Investigating the sources of atmospheric nitrous acid (HONO) in the megacity of Beijing, China. *Science of the Total Environment*, *812*, 152270. https://doi.org/10.1016/j.scitotenv.2021.152270

Guenther, A., Karl, T., Harley, P., Wiedinmyer, C., Palmer, P. I., & Geron, C. (2006). Estimates of global terrestrial isoprene emissions using MEGAN (model of emissions of gases and aerosols from nature). *Atmospheric Chemistry and Physics*, *6*(11), 3181–3210. https://doi.org/10.5194/acp-6-3181-2006

Hersbach, H., Bell, B., Berrisford, P., Biavati, G., Horányi, A., Muñoz Sabater, J., et al. (2023). ERA5 hourly data on single levels from 1940 to present. *Copernic. Clim. Change Serv. C3S Clim. Data Store CDS*. https://doi.org/10.24381/cds.adbb2d47

Huang, X., Ding, A., Gao, J., Zheng, B., Zhou, D., Qi, X., et al. (2021). Enhanced secondary pollution offset reduction of primary emissions during COVID-19 lockdown in China. *National Science Review*, *8*(2), nwaa137. https://doi.org/10.1093/nsr/nwaa137

Huang, X., Ding, A., Wang, Z., Ding, K., Gao, J., Chai, F., & Fu, C. (2020). Amplified transboundary transport of haze by aerosol–boundary layer interaction in China. *Nature Geoscience*, *13*(6), 428–434. https://doi.org/10.1038/s41561-020-0583-4

Ji, Y., Qin, X., Wang, B., Xu, J., Shen, J., Chen, J., et al. (2018). Counteractive effects of regional transport and emission control on the formation of fine particles: A case study during the Hangzhou G20 summit. *Atmospheric Chemistry and Physics*, *18*, 13581–13600. https://doi.org/10.5194/acp-18-13581-2018

Kang, H., Zhu, B., Liu, X., Shi, S., Hou, X., Lu, W., et al. (2021). Three-dimensional distribution of PM2.5 over the Yangtze River Delta as cold fronts moving through. *Journal of Geophysical Research: Atmospheres*, *126*(8), e2020JD034035. https://doi.org/10.1029/2020JD034035

Kim, S., VandenBoer, T. C., Young, C. J., Riedel, T. P., Thornton, J. A., Swarthout, B., et al. (2014). The primary and recycling sources of OH during the NACHTT-2011 campaign: HONO as an important OH primary source in the wintertime. *Journal of Geophysical Research: Atmospheres*, *119*(11), 6886–6896. https://doi.org/10.1002/2013JD019784

Kleffmann, J., Gavriloaiei, T., Hofzumahaus, A., Holland, F., Koppmann, R., Rupp, L., et al. (2005). Daytime formation of nitrous acid: A major source of OH radicals in a forest. *Geophysical Research Letters*, *32*(5). https://doi.org/10.1029/2005GL022524

Kurtenbach, R., Becker, K. H., Gomes, J. A. G., Kleffmann, J., Lörzer, J. C., Spittler, M., et al. (2001). Investigations of emissions and heterogeneous formation of HONO in a road traffic tunnel. *Atmospheric Environment*, *35*(20), 3385–3394. https://doi.org/10.1016/S1352-2310(01)00138-8

Li, G., Lei, W., Zavala, M., Volkamer, R., Dusanter, S., Stevens, P., & Molina, L. T. (2010). Impacts of HONO sources on the photochemistry in Mexico City during the MCMA-2006/MILAGO Campaign. *Atmospheric Chemistry and Physics*, *10*(14), 6551–6567. https://doi.org/10.5194/acp-10-6551-2010

Li, K., Jacob, D. J., Liao, H., Shen, L., Zhang, Q., & Bates, K. H. (2019). Anthropogenic drivers of 2013–2017 trends in summer surface ozone in China. *Proceedings of the National Academy of Sciences*, *116*(2), 422–427. https://doi.org/10.1073/pnas.1812168116

Li, M., Zhang, Q., Kurokawa, J., Woo, J.-H., He, K., Lu, Z., et al. (2017). MIX: A mosaic Asian anthropogenic emission inventory under the international collaboration framework of the MICS-Asia and HTAP. *Atmospheric Chemistry and Physics*, *17*(2), 935–963. https://doi.org/10.5194/acp-17-935-2017

Li, N., Zhang, H., Zhu, S., Liao, H., Hu, J., Tang, K., et al. (2023). Secondary PM2.5 dominates aerosol pollution in the Yangtze River Delta region: Environmental and health effects of the Clean air Plan. *Environment International*, *171*, 107725. https://doi.org/10.1016/j.envint.2022.107725

Li, X., Bei, N., Wu, J., Wang, R., Liu, S., Liu, L., et al. (2022). Heterogeneous HONO formation deteriorates the wintertime particulate pollution in the Guanzhong Basin, China. *Environmental Pollution*, *303*, 119157. https://doi.org/10.1016/j.envpol.2022.119157

Liao, S., Zhang, J., Yu, F., Zhu, M., Liu, J., Ou, J., et al. (2021). High gaseous nitrous acid (HONO) emissions from light-duty diesel vehicles. *Environmental Science and Technology*, *55*(1), 200–208. https://doi.org/10.1021/acs.est.0c05599

Liu, J., Liu, Z., Ma, Z., Yang, S., Yao, D., Zhao, S., et al. (2021). Detailed budget analysis of HONO in Beijing, China: Implication on atmosphere oxidation capacity in polluted megacity. *Atmospheric Environment*, *244*, 117957. https://doi.org/10.1016/j.atmosenv.2020.117957

Liu, L., Bei, N., Hu, B., Wu, J., Liu, S., Li, X., et al. (2020). Wintertime nitrate formation pathways in the north China plain: Importance of N2O5 heterogeneous hydrolysis. *Environmental Pollution*, *266*, 115287. https://doi.org/10.1016/j.envpol.2020.115287

Liu, X., Zhu, B., Zhu, T., & Liao, H. (2022). The Seesaw pattern of PM2.5 Interannual anomalies between Beijing-Tianjin-Hebei and Yangtze River Delta across eastern China in winter. *Geophysical Research Letters*, *49*(2), e2021GL095878. https://doi.org/10.1029/2021GL095878

Liu, Y., Lu, K., Li, X., Dong, H., Tan, Z., Wang, H., et al. (2019). A comprehensive model test of the HONO sources constrained to field measurements at rural north China plain. *Environmental Science and Technology*, *53*(7), 3517–3525. https://doi.org/10.1021/acs.est.8b06367

Liu, Y., Nie, W., Xu, Z., Wang, T., Wang, R., Li, Y., et al. (2019). Semi-quantitative understanding of source contribution to nitrous acid (HONO) based on 1 year of continuous observation at the SORPES station in eastern China. *Atmospheric Chemistry and Physics*, *19*(20), 13289–13308. https://doi.org/10.5194/acp-19-13289-2019

Lu, X., Zhang, L., Wang, X., Gao, M., Li, K., Zhang, Y., et al. (2020). Rapid increases in warm-season surface ozone and resulting health impact in China since 2013. *Environmental Science and Technology Letters*, *7*(4), 240–247. https://doi.org/10.1021/acs.estlett.0c00171

Ma, X., Tan, Z., Lu, K., Yang, X., Chen, X., Wang, H., et al. (2022). OH and HO_2 radical chemistry at a suburban site during the EXPLORE-YRD campaign in 2018. *Atmospheric Chemistry and Physics*, *22*(10), 7005–7028. https://doi.org/10.5194/acp-22-7005-2022

Miao, R., Chen, Q., Shrivastava, M., Chen, Y., Zhang, L., Hu, J., et al. (2021). Process-based and observation-constrained SOA simulations in China: The role of semivolatile and intermediate-volatility organic compounds and OH levels. *Atmospheric Chemistry and Physics*, *21*, 16183–16201. https://doi.org/10.5194/acp-21-16183-2021

Monge, M. E., D'Anna, B., Mazri, L., Giroir-Fendler, A., Ammann, M., Donaldson, D. J., & George, C. (2010). Light changes the atmospheric reactivity of soot. *Proceedings of the National Academy of Sciences*, *107*(15), 6605–6609. https://doi.org/10.1073/pnas.0908341107

Nie, W., Ding, A. J., Xie, Y. N., Xu, Z., Mao, H., Kerminen, V.-M., et al. (2015). Influence of biomass burning plumes on HONO chemistry in eastern China. *Atmospheric Chemistry and Physics*, *15*(3), 1147–1159. https://doi.org/10.5194/acp-15-1147-2015

Oswald, R., Behrendt, T., Ermel, M., Wu, D., Su, H., Cheng, Y., et al. (2013). HONO emissions from soil bacteria as a major source of atmospheric reactive nitrogen. *Science*, *341*(6151), 1233–1235. https://doi.org/10.1126/science.1242266

Sarwar, G., Roselle, S. J., Mathur, R., Appel, W., Dennis, R. L., & Vogel, B. (2008). A comparison of CMAQ HONO predictions with observations from the northeast oxidant and particle study. *Atmospheric Environment*, *42*(23), 5760–5770. https://doi.org/10.1016/j.atmosenv.2007.12.065

Slater, E. J., Whalley, L. K., Woodward-Massey, R., Ye, C., Lee, J. D., Squires, F., et al. (2020). Elevated levels of OH observed in haze events during wintertime in central Beijing. *Atmospheric Chemistry and Physics*, *20*(23), 14847–14871. https://doi.org/10.5194/acp-20-14847-2020

Song, M., Zhao, X., Liu, P., Mu, J., He, G., Zhang, C., et al. (2023). Atmospheric NOx oxidation as major sources for nitrous acid (HONO). *npj Climate and Atmospheric Science*, *6*(1), 30. https://doi.org/10.1038/s41612-023-00357-8

Song, Y., Zhang, Y., Xue, C., Liu, P., He, X., Li, X., & Mu, Y. (2022). The seasonal variations and potential sources of nitrous acid (HONO) in the rural North China Plain. *Environmental Pollution*, *311*, 119967. https://doi.org/10.1016/j.envpol.2022.119967

Su, H., Cheng, Y., Oswald, R., Behrendt, T., Trebs, I., Meixner, F. X., et al. (2011). Soil nitrite as a source of atmospheric HONO and OH radicals. *Science*, *333*(6049), 1616–1618. https://doi.org/10.1126/science.1207687

Su, H., Cheng, Y. F., Shao, M., Gao, D. F., Yu, Z. Y., Zeng, L. M., et al. (2008). Nitrous acid (HONO) and its daytime sources at a rural site during the 2004 PRIDE-PRD experiment in China. *Journal of Geophysical Research*, *113*(D14). https://doi.org/10.1029/2007JD009060

Sun, P., Nie, W., Chi, X., Xie, Y., Huang, X., Xu, Z., et al. (2018). Two years of online measurement of fine particulate nitrate in the western Yangtze River Delta: Influences of thermodynamics and N_2O_5 hydrolysis. *Atmospheric Chemistry and Physics*, *18*(23), 17177–17190. https://doi.org/10.5194/acp-18-17177-2018

Tan, W., Wang, H., Su, J., Sun, R., He, C., Lu, X., et al. (2023). Soil emissions of reactive nitrogen accelerate summertime surface ozone increases in the North China plain. *Environmental Science and Technology*, *57*(34), 12782–12793. https://doi.org/10.1021/acs.est.3c01823

Tang, K., Zhang, H., Feng, W., Liao, H., Hu, J., & Li, N. (2022). Increasing but variable trend of surface ozone in the Yangtze River Delta region of China. *Frontiers of Environmental Science*, *10*, 836191. https://doi.org/10.3389/fenvs.2022.836191

Theys, N., Volkamer, R., Müller, J.-F., Zarzana, K. J., Kille, N., Clarisse, L., et al. (2020). Global nitrous acid emissions and levels of regional oxidants enhanced by wildfires. *Nature Geoscience*, *13*(10), 681–686. https://doi.org/10.1038/s41561-020-0637-7

Wang, H., Wang, H., Lu, X., Lu, K., Zhang, L., Tham, Y. J., et al. (2023). Increased night-time oxidation over China despite widespread decrease across the globe. *Nature Geoscience*, *16*(3), 217–223. https://doi.org/10.1038/s41561-022-01122-x

Wang, T., Xue, L., Brimblecombe, P., Lam, Y. F., Li, L., & Zhang, L. (2017). Ozone pollution in China: A review of concentrations, meteorological influences, chemical precursors, and effects. *Science of the Total Environment*, *575*, 1582–1596. https://doi.org/10.1016/j.scitotenv.2016.10.081

Wang, W., Li, X., Cheng, Y., Parrish, D. D., Ni, R., Tan, Z., et al. (2023). Ozone pollution mitigation strategy informed by long-term trends of atmospheric oxidation capacity. *Nature Geoscience*, *17*, 1–6. https://doi.org/10.1038/s41561-023-01334-9

Xia, M., Peng, X., Wang, W., Yu, C., Sun, P., Li, Y., et al. (2020). Significant production of $ClNO_2$ and possible source of Cl_2 from N_2O_5 uptake at a suburban site in eastern China. *Atmospheric Chemistry and Physics*, *20*(10), 6147–6158. https://doi.org/10.5194/acp-20-6147-2020

Xing, L., Wu, J., Elser, M., Tong, S., Liu, S., Li, X., et al. (2019). Wintertime secondary organic aerosol formation in Beijing–Tianjin–Hebei (BTH): Contributions of HONO sources and heterogeneous reactions. *Atmospheric Chemistry and Physics*, *19*(4), 2343–2359. https://doi.org/10.5194/acp-19-2343-2019

Xu, Z., Wang, T., Wu, J., Xue, L., Chan, J., Zha, Q., et al. (2015). Nitrous acid (HONO) in a polluted subtropical atmosphere: Seasonal variability, direct vehicle emissions and heterogeneous production at ground surface. *Atmospheric Environment*, *106*, 100–109. https://doi.org/10.1016/j.atmosenv.2015.01.061

Xuan, H., Zhao, Y., Ma, Q., Chen, T., Liu, J., Wang, Y., et al. (2023). Formation mechanisms and atmospheric implications of summertime nitrous acid (HONO) during clean, ozone pollution and double high-level PM2.5 and O3 pollution periods in Beijing. *Science of the Total Environment*, *857*, 159538. https://doi.org/10.1016/j.scitotenv.2022.159538

Xue, C. (2022). Substantially growing interest in the chemistry of nitrous acid (HONO) in China: Current achievements, problems, and future directions. *Environmental Science and Technology*, *56*(12), 7375–7377. https://doi.org/10.1021/acs.est.2c02237

Xue, C., Ye, C., Zhang, C., Catoire, V., Liu, P., Gu, R., et al. (2021). Evidence for strong HONO emission from fertilized agricultural fields and its remarkable impact on regional O_3 pollution in the summer north China plain. *ACS Earth and Space Chemistry*, *5*(2), 340–347. https://doi.org/10.1021/acsearthspacechem.0c00314

Ye, C., Lu, K., Ma, X., Qiu, W., Li, S., Yang, X., et al. (2023). HONO chemistry at a suburban site during the EXPLORE-YRD campaign in 2018: Formation mechanisms and impacts on O_3 production. *Atmospheric Chemistry and Physics*, *23*(24), 15455–15472. https://doi.org/10.5194/acp-23-15455-2023

Ye, C., Zhang, N., Gao, H., & Zhou, X. (2017). Photolysis of particulate nitrate as a source of HONO and NOx. *Environmental Science and Technology*, *51*(12), 6849–6856. https://doi.org/10.1021/acs.est.7b00387

Ye, C., Zhou, X., Pu, D., Stutz, J., Festa, J., Spolaor, M., et al. (2016). Rapid cycling of reactive nitrogen in the marine boundary layer. *Nature*, *532*(7600), 489–491. https://doi.org/10.1038/nature17195

Yu, C., Huang, L., Xue, L., Shen, H., Li, Z., Zhao, M., et al. (2022). Photoenhanced heterogeneous uptake of NO_2 and HONO formation on authentic winter time urban grime. *ACS Earth and Space Chemistry*, *6*(8), 1960–1968. https://doi.org/10.1021/acsearthspacechem.2c00054

Zaveri, R. A., Easter, R. C., Fast, J. D., & Peters, L. K. (2008). Model for simulating aerosol interactions and chemistry (MOSAIC). *Journal of Geophysical Research*, *113*(D13), D13204. https://doi.org/10.1029/2007JD008782

Zhang, H., & Huang, X. (2024). HONO observations and model data at SORPES station, Nanjing during March 24 to 27, 2019 [Dataset]. *figshare*. https://doi.org/10.6084/m9.figshare.25782471.v2

Zhang, J., An, J., Qu, Y., Liu, X., & Chen, Y. (2019). Impacts of potential HONO sources on the concentrations of oxidants and secondary organic aerosols in the Beijing-Tianjin-Hebei region of China. *Science of the Total Environment*, *647*, 836–852. https://doi.org/10.1016/j.scitotenv.2018.08.030

Zhang, J., Chen, J., Xue, C., Chen, H., Zhang, Q., Liu, X., et al. (2019). Impacts of six potential HONO sources on HOx budgets and SOA formation during a wintertime heavy haze period in the North China Plain. *Science of the Total Environment*, *681*, 110–123. https://doi.org/10.1016/j.scitotenv.2019.05.100

Zhang, J., Lian, C., Wang, W., Ge, M., Guo, Y., Ran, H., et al. (2022a). Amplified role of potential HONO sources in O3 formation in North China Plain during autumn haze aggravating processes. *Atmospheric Chemistry and Physics*, *22*(5), 3275–3302. https://doi.org/10.5194/acp-22-3275-2022

Zhang, J., Ran, H., Guo, Y., Xue, C., Liu, X., Qu, Y., et al. (2022b). High crop yield losses induced by potential HONO sources—A modelling study in the North China plain. *Science of the Total Environment*, *803*, 149929. https://doi.org/10.1016/j.scitotenv.2021.149929

Zhang, L., Wang, T., Zhang, Q., Zheng, J., Xu, Z., & Lv, M. (2016). Potential sources of nitrous acid (HONO) and their impacts on ozone: A WRF-Chem study in a polluted subtropical region. *Journal of Geophysical Research: Atmospheres*, *121*(7), 3645–3662. https://doi.org/10.1002/2015JD024468

Zhang, Q., Liu, P., Wang, Y., George, C., Chen, T., Ma, S., et al. (2023a). Unveiling the underestimated direct emissions of nitrous acid (HONO). *Proceedings of the National Academy of Sciences*, *120*(35), e2302048120. https://doi.org/10.1073/pnas.2302048120

Zhang, S., Sarwar, G., Xing, J., Chu, B., Xue, C., Sarav, A., et al. (2021). Improving the representation of HONO chemistry in CMAQ and examining its impact on haze over China. *Atmospheric Chemistry and Physics*, *21*(20), 15809–15826. https://doi.org/10.5194/acp-21-15809-2021

Zhang, X., Tong, S., Jia, C., Zhang, W., Li, J., Wang, W., et al. (2022c). The levels and sources of nitrous acid (HONO) in winter of Beijing and Sanmenxia. *Journal of Geophysical Research: Atmospheres*, *127*(10), e2021JD036278. https://doi.org/10.1029/2021JD036278

Zhang, X., Tong, S., Jia, C., Zhang, W., Wang, Z., Tang, G., et al. (2023b). Elucidating HONO formation mechanism and its essential contribution to OH during haze events. *npj Climate and Atmospheric Science*, *6*(1), 55. https://doi.org/10.1038/s41612-023-00371-w

Zhao, X., Zhao, X., Liu, P., Chen, D., Zhang, C., Xue, C., et al. (2023). Transport pathways of nitrate formed from nocturnal N_2O_5 hydrolysis Aloft to the ground level in winter north China plain. *Environmental Science and Technology*, *57*(7), 2715–2725. https://doi.org/10.1021/acs.est.3c00086

Zheng, J., Shi, X., Ma, Y., Ren, X., Jabbour, H., Diao, Y., et al. (2020). Contribution of nitrous acid to the atmospheric oxidation capacity in an industrial zone in the Yangtze River Delta region of China. *Atmospheric Chemistry and Physics*, *20*(9), 5457–5475. https://doi.org/10.5194/acp-20-5457-2020

Zhou, X., Huang, X., Sun, P., Chi, X., Ren, C., Lai, S., et al. (2023). Fast secondary aerosol formation in residual layer and its impact on air pollution over eastern China. *Journal of Geophysical Research: Atmospheres*, *128*(11), e2023JD038501. https://doi.org/10.1029/2023JD038501

References From the Supporting Information

Chen, F., & Dudhia, J. (2001). Coupling and advanced land surface-hydrology model with the Penn State-NCAR MM5 modeling system. Part I: Model implementation and sensitivity. *Monthly Weather Review*, *129*(4), 569–585. https://doi.org/10.1175/1520-0493(2001)129<0569:CAALSH>2.0.CO;2

Grell, G. A., & Dévényi, D. (2002). A generalized approach to parameterizing convection combining ensemble and data assimilation techniques. *Geophysical Research Letters*, *29*(14). https://doi.org/10.1029/2002GL015311

Iacono, M. J., Delamere, J. S., Mlawer, E. J., Shephard, M. W., Clough, S. A., & Collins, W. D. (2008). Radiative forcing by long-lived greenhouse gases: Calculations with the AER radiative transfer models. *Journal of Geophysical Research*, *113*(D13). https://doi.org/10.1029/2008JD009944

Jiménez, P. A., Dudhia, J., González-Rouco, J. F., Navarro, J., Montávez, J. P., & García-Bustamante, E. (2012). A revised scheme for the WRF surface layer formulation. *Monthly Weather Review*, *140*(3), 898–918. https://doi.org/10.1175/MWR-D-11-00056.1

Morrison, H., Thompson, G., & Tatarskii, V. (2009). Impact of cloud microphysics on the development of Trailing Stratiform precipitation in a simulated squall line: Comparison of one- and two-moment schemes. *Monthly Weather Review*, *137*(3), 991–1007. https://doi.org/10.1175/2008MWR2556.1

Nakanishi, M., & Niino, H. (2006). An improved Mellor–Yamada level-3 model: Its numerical stability and application to a regional prediction of advection Fog. *Boundary-Layer Meteorology*, *119*(2), 397–407. https://doi.org/10.1007/s10546-005-9030-8

Shrivastava, M., Fast, J., Easter, R., Gustafson, W. I. J., Zaveri, R. A., Jimenez, J. L., et al. (2011). Modeling organic aerosols in a megacity: Comparison of simple and complex representations of the volatility basis set approach. *Atmospheric Chemistry and Physics*, *11*(13), 6639–6662. https://doi.org/10.5194/acp-11-6639-2011

Wild, O., Zhu, X., & Prather, M. J. (2000). Fast-J: Accurate simulation of in- and below-cloud photolysis in tropospheric chemical models. *Journal of Atmospheric Chemistry*, *37*(3), 245–282. https://doi.org/10.1023/A:1006415919030

Wong, K. W., Tsai, C., Lefer, B., Grossberg, N., & Stutz, J. (2013). Modeling of daytime HONO vertical gradients during SHARP 2009. *Atmospheric Chemistry and Physics*, *13*(7), 3587–3601. https://doi.org/10.5194/acp-13-3587-2013

Zhang, W., Tong, S., Jia, C., Ge, M., Ji, D., Zhang, C., et al. (2022d). Effect of different combustion processes on atmospheric nitrous acid formation mechanisms: A winter comparative observation in urban, suburban and rural areas of the North China plain. *Environmental Science and Technology*, *56*(8), 4828–4837. https://doi.org/10.1021/acs.est.1c07784

Zhang, W., Tong, S., Lin, D., Li, F., Zhang, X., Wang, L., et al. (2023). Atmospheric chemistry of nitrous acid and its effects on hydroxyl radical and ozone at the urban area of Beijing in early spring 2021. *Environmental Pollution*, *316*, 120710. https://doi.org/10.1016/j.envpol.2022.120710